Mechanism of long-lasting phosphorescence process of Ce^{3+}-doped $Ca_2Al_2SiO_7$ melilite crystals

Mitsuo Yamaga and Yoshifumi Tanii
Department of Electrical and Electronic Engineering, Faculty of Engineering, Gifu University, Gifu, 501-1193, Japan

Nobuhiro Kodama and Tomoko Takahashi
Department of Materials Science and Engineering, Faculty of Engineering and Resource Science, Akita University, Akita, 010-8502, Japan

Makoto Honda
Faculty of Science, Naruto University of Education, Naruto, 772-8502, Japan
(Received 22 December 2001; published 4 June 2002)

UV excitation of Ce^{3+}-doped $Ca_2Al_2SiO_7$ melilite crystals produces long-lasting phosphorescence ($1\text{-}10^3$ s) from Ce^{3+} ions in addition to the intrinsic Ce^{3+} luminescence with a lifetime of 40 ns. The distribution of the radiative decay rates is due to recombination of distant pairs of electron and hole in the crystals. The electron spin-resonance study gives evidence that pairs of electron and hole are produced through UV excitation of Ce^{3+} in the crystals and that electrons are trapped at O^{2-} vacancies as F^+ centers, the wave functions extending toward Al^{3+} ions, while holes are self-trapped at Al^{3+} ions accompanied by Si^{4+} vacancies in the nearest neighbors along the $\langle 110\rangle$ or $\langle \bar{1}10\rangle$ direction. The intensities of the phosphorescence at the peak wavelength of 410 nm were measured as functions of temperature and time. The decay curves of the phosphorescence at various temperatures fit $t^{-n}(n<1)$. The temperature dependence of the intensities integrated in a time domain obeys the Arrhenius' equation with a thermal activation energy of 243 meV. These results support that the self-trapped holes Al^{4+} produced in the crystal by the UV excitation of Ce^{3+} move back to Ce^{3+} sites through tunneling and thermal hopping, and the retrapped holes in the form of Ce^{4+} recombine radiatively the trapped electrons through tunneling.

DOI: 10.1103/PhysRevB.65.235108 PACS number(s): 78.55.−m, 76.30.−v, 76.30.Kg, 78.20.−e

I. INTRODUCTION

Rare-earth ions doped materials are good candidates for photonic sources.[1] Trivalent rare-earth ions Ce^{3+} in ionic crystals are regarded as optically active ions, which emit in the range of the UV and visible.[1,2] The electronic configurations of the ground and excited states of Ce^{3+} in crystals are $4f^1$ and $5d^1$, respectively. The absorption and luminescence transitions between these states are allowed electric-dipole transitions, resulting in large absorption coefficients and short luminescence lifetimes of a few tens ns. Laser operation in the UV range has been reported based on the $5d \rightarrow 4f$ transition of Ce^{3+} in $LiYF_4$ (Refs. 2,3) and $LiCaAlF_6$,[4] whereas lasing using Ce^{3+}-doped oxides, for example, $Y_3Al_5O_{12}(YAG):Ce^{3+}$ (Ref. 5) was not successful because of the large excited state absorption.

Divalent rare-earth ions Eu^{2+} in crystals have the $4f^7$ and $4f^65d^1$ electronic configurations of the ground and excited states, respectively.[1] The broadband absorption and luminescence of Eu^{2+} in crystals are due to the $4f^7 \leftrightarrow 4f^65d^1$ transitions. The optical feature is very similar to that of Ce^{3+}. The $5d \rightarrow 4f$ transition of Eu^{2+} is also spin and parity allowed and the lifetime is submicroseconds, being several times longer than that of Ce^{3+}.[1] Long-lasting phosphorescence in the blue/green and yellow regions has been observed in alkaline-earth aluminates $Sr_4Al_{14}O_{25}:Eu^{2+}:Dy^{3+}$ and $SrAl_2O_4:Eu^{2+}:Dy^{3+}$, respectively.[6] The lifetimes of the phosphorescence in these crystals vary in the range of $1-10^4$ s. This feature, being different from the intrinsic radiative decay of Eu^{2+}, is explained by recombination of electron-hole pairs created by optical excitation, where Dy^{3+} ions play a role as a hole-trapped center. The distribution of distances between trapped electrons and holes may give rise to the variation of the lifetimes.

We have grown Ce^{3+}-doped $Ca_2Al_2SiO_7$ melilite crystals which are candidates for tunable solid state laser materials in the violet and blue regions.[7] First observation of long-lasting phosphorescence in the violet and blue regions using the Ce^{3+}-doped $Ca_2Al_2SiO_7$ crystals was reported.[8] In order to understand the phosphorescence, we have examined the local structure of electrons and holes produced in the crystals by UV excitation using the electron spin-resonance (ESR) technique and the properties of the phosphorescence as functions of temperature and time using a conventional optical technique. In this paper, we have proposed a mechanism of the long-lasting phosphorescence process based on coupled pairs of electron and hole produced in the crystals by the UV excitation.

II. EXPERIMENTAL PROCEDURE

$Ca_2Al_2SiO_7$ (CASM) crystals have the melilite structure (tetragonal sheet structure) with space group D_{2d}^3 as shown in Fig. 1.[9] The sheet structure in CASM consists of five numbered rings of TO_4 ($T=Al^{3+}$, Si^{4+}) tetrahedra perpendicular to the c axis. Tetrahedra 1 and 4 are occupied by Al(1) ions, whereas tetrahedra 2, 3, and 5 are randomly occupied by Al(2) and Si ions keeping a composition ratio of 1:1. There are three O^{2-} sites with different symmetry, de-

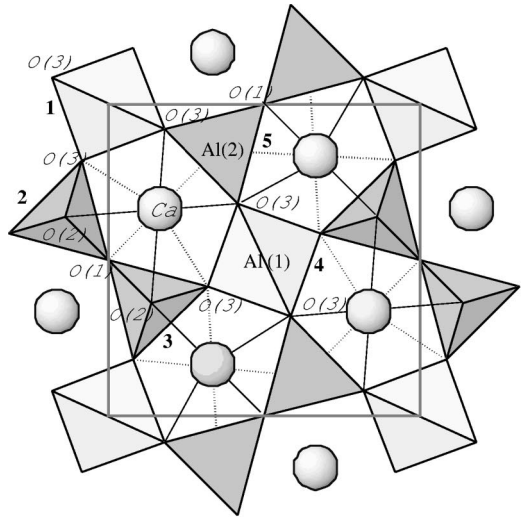

(a) Projection to the (001) plane

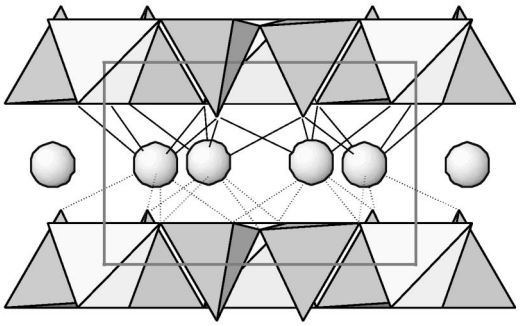

(b) Projection to the (010) plane

FIG. 1. The projections of the crystal structure of $Ca_2Al_2SiO_7$ in (a) the (001) plane and (b) the (010) plane. [O(1), O(2), O(3)] and [Al(1), Al(2)] denote lattice sites of oxygen and aluminum with different symmetry. Ca^{2+} ions are eightfold coordinated. The dashed and solid lines represent the directions from a Ca^{2+} ion to the four nearest neighbor O^{2-} ligand ions in each (001) plane.

noted by O(1), O(2), and O(3). Two apexes, O(2) ions, of the tetrahedra 2 and 3, two obliques combining with two O(3) ions in the tetrahedra 1 and 4, and a plane containing one O(1) and two O(3) ions in the tetrahedron 5 are located in the same (001) plane as shown in Fig. 1(a). Ca^{2+} ions are sandwiched between these rings and eightfold coordinated as shown in Fig. 1(b). The directions from a Ca^{2+} ion to the four nearest neighbor O^{2-} ligand ions in each (001) plane are denoted by solid or dashed lines in Fig. 1. One of the two planes is rotated with an amount of $\sim 45°$ around the crystalline *c* axis so that Ca^{2+} complexes have C_s symmetry. There are four structurally equivalent Ca^{2+} complexes in a unit cell with mirror symmetry with respect to the (100) and (010) planes.

The CASM crystals were grown containing nominally 0.05 at.% Ce^{3+} relative to Ca^{2+} by the Czochralski technique. Ce^{3+} ions substitute for Ca^{2+} ions. The composition was determined to be $Ce_{0.001}Ca_{1.998}Al_2Si_{0.90}O_{6.80}$ by the inductively coupled plasma (ICP) technique. The concentrations of Si^{4+} and O^{2-} vacancies in the crystals were estimated to be ~ 10 and ~ 3 %, respectively. They changed slightly at the crystal positions along the direction of the crystal growth.

ESR measurements were carried out using a JES-FA200 *X*-band spectrometer with microwave frequencies of ~ 9.182 and ~ 9.066 GHz at 77 and 293 K, respectively. Low-temperature ESR spectra were measured using a Bruker EMX10/12 *X*-band spectrometer with ~ 9.687 GHz in the temperature range of 5–300 K. Both spectrometers employed 100 kHz field modulation.

Optical absorption spectra were measured at 293 K using a Hitachi U-3500 spectrometer in the range of 180–2500 nm. Luminescence spectra under steady-state excitation were measured at 293 K using a Hitachi F-4500 fluorescence spectrophotometer. Lifetimes of the luminescence were measured using a Horiba NAES-700F time-resolved photoluminescence spectrometer in the temperature range of 77–400 K in Instrumental Analysis Center, Gifu University. Long-lasting phosphorescence was measured as follows. The sample was excited for five minutes with the laser light obtained from the third harmonics (355 nm) of a pulsed Nd-YAG laser. The measurement of the phosphorescence intensities started at 5 s after removal of the excitation light. Optical signals passing through a 1/4 m monochromator were detected by a Hamamatsu Photonics R943-02 photomultiplier and a Keithley 428 current amplifier. The signals were sampled with 10 kHz, integrated in a period of 1 s, and changed to digital signals using a Stanford Research Systems SR250 boxcar average controlled by a personal computer. Then, thousand data were stored in the personal computer. Sample temperatures below and above 293 K were achieved using a cryorefrigerator and a hot plate with temperature control, respectively.

III. EXPERIMENTAL RESULTS

A. ESR measurements

Figure 2 show the ESR spectra observed for the as-grown CASM:Ce crystal with the magnetic field applied parallel to the $\langle 100\rangle$, $\langle 110\rangle$, and $\langle 001\rangle$ axes at 5 K with a microwave power of 0.01 mW and microwave frequencies of 9.694, 9.684, and 9.687 GHz, respectively. The spectrum with $\mathbf{B}\|\langle 001\rangle$ consists of fairly broad resonance lines spread in the range of 0.8–1.5 T, denoted by *A*, and six sharp and weak resonance lines at 0.3–0.4 T, denoted by *B*. The *A* signals for $\mathbf{B}\|\langle 100\rangle$ and $\langle 110\rangle$ are shifted to lower fields and clearly split into two components. The splitting with $\mathbf{B}\|\langle 110\rangle$ is much larger than that with $\mathbf{B}\|\langle 100\rangle$. The positions and separations of the *B* signals are almost the same for the three magnetic field directions. The line shapes of the *A* and *B* signals have only positive components of the first derivative, even when a microwave power is reduced to ~ 1 μW. Such phenomena occur for resonance measured under conditions of rapid passage, in which a sweep rate of magnetic field is much faster than a spin-lattice relaxation rate.[10] Isotropic ESR signals with sharp and perfect derivative curves, denoted by an asterisk, are due to impurities in a cavity.

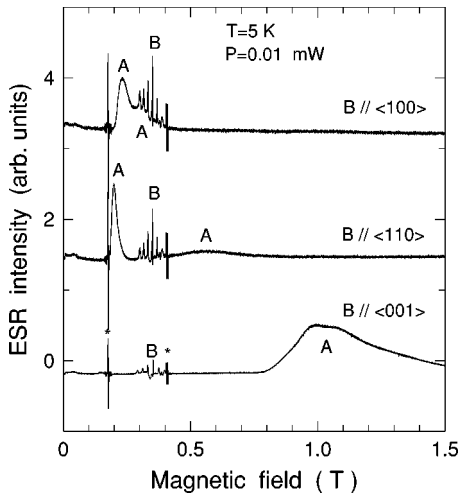

FIG. 2. The ESR spectra of the as-grown $Ca_2Al_2SiO_7$:Ce crystal with $\mathbf{B}\|\langle 100\rangle$, $\langle 110\rangle$, and $\langle 001\rangle$ at 5 K with a microwave power of 0.01 mW and microwave frequencies of 9.687, 9.684, and 9.694 GHz, respectively. The broad and sextet lines are denoted by *A* and *B*, respectively. Isotropic signals denoted by an asterisk are due to impurities in a cavity.

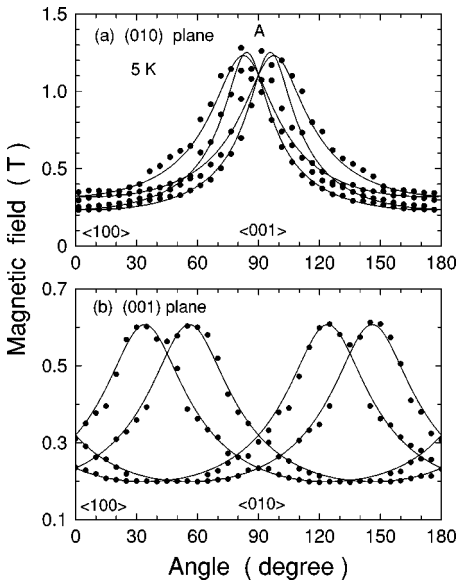

FIG. 3. The angular variations of the *A* signals for $Ca_2Al_2SiO_7$:Ce measured at 5 K in (a) the (010) plane and (b) the (001) plane. The solid curves are calculated using Eq. (1) and the parameters of the *A* center in Table I.

In increasing temperatures, the negative component of the broad *A* signal appeared at ~ 15 K. The line was broadened, rapidly decreased in intensity, and disappeared completely above 20 K. As *g* values are determined by resonance-field positions where the first derivative changes from positive to negative, it is very difficult to estimate *g* values from only broad positive components of the *A* signals in Fig. 2 or very weak and broad derivative at 15–20 K. In a previous paper,[11] Yamaga *et al.* showed that in a system with adiabatic rapid passage, for example, in Ce^{3+}-doped $CaYAlO_4$, the broad spectrum with only positive component of the first derivative is experimentally coincident with the microwave absorption. As a consequence, the peaks of the positive components are equal to the resonance fields. The angular variations of the *A* signals in the (010) and (001) planes were shown in Fig. 3. The patterns show orthorhombic symmetry.

The angular dependence of the *A* signal fits curves calculated using the spin Hamiltonian with orthorhombic symmetry in the form[12]

$$\mathcal{H}=\mu_B g_x B_x S_x+\mu_B g_y B_y S_y+\mu_B g_z B_z S_z, \qquad (1)$$

where μ_B is the Bohr magneton, *B* is a resonance magnetic field, and $S(=\frac{1}{2})$ is an effective spin. In order to define the principal *x*, *y*, and *z* axes of orthorhombic centers, the crystalline *a*, *b*, and *c* axes are rotated around an arbitrary direction. This is achieved through a succession of three rotations: a first rotation by an angle ϕ about the *c* axis, the new axes being a', b', and $c'(=c)$; a second rotation by an angle θ about the b' axis, the new axes being a'', $b''(=b')$, and c''; and a third rotation by angle ψ about the c'' axis. The final axes are defined as the *x*, *y*, and *z* axes of the *g* tensor, respectively. The *z* axis as determined experimentally is found to be substantially different two other *g* values. The solid curves in Fig. 3, calculated using Eq. (1) and the parameters of *A* center in Table I are in good agreement with the experimental points. The four structurally equivalent and magnetically inequivalent centers are consistent with the four Ca^{2+} complexes in the unit cell of the melilite crystal structure in Fig. 1. As the line shapes and the *g* values of the *A* center are very similar to those of Ce^{3+} in $CaYAlO_4$,[11] the *A* center is assigned to Ce^{3+} ions substituting for Ca^{2+} ions with orthorhombic symmetry reflecting the melilite crystal structure.

Figure 4 shows the temperature dependence of the ESR spectra with $\mathbf{B}\|\langle 100\rangle$ and a microwave power of 1 μW in the range of 5–100 K. The *A* signal disappeared completely at 5 K with decreasing the microwave power down to 1 μW

TABLE I. The spin Hamiltonian parameters in Eqs. (1) and (2) for *A*, *B*, and *C* centers observed in the $Ca_2Al_2SiO_7$:Ce melilite crystals.

centers	*A*	*B*	*C*
g values			
$g_x(g_\perp)$	3.48(2)	2.000(5)	2.052(5)
g_y	1.14(2)		2.020(3)
$g_z(g_\parallel)$	0.55(5)	2.003(5)	2.003(3)
h.f. coupling constants (MHz)			
$A_x(A_\perp)$		490	25
A_y			31
$A_z(A_\parallel)$		590	31
polar angles (deg)			
θ	± 5	0	90
ϕ	± 34	0	± 45
ψ	0	0	0
temperatures (K)	5	5	77

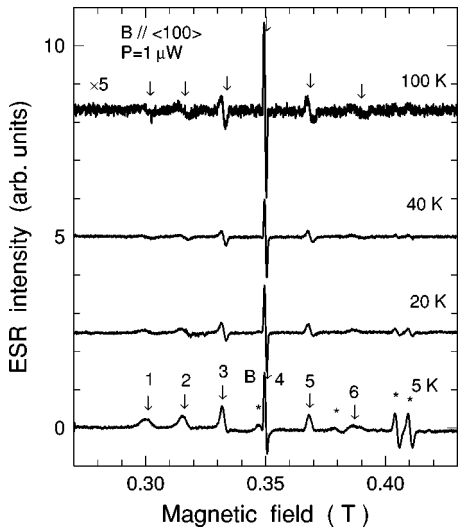

FIG. 4. The temperature dependence of the *B* signal of $Ca_2Al_2SiO_7$:Ce with $\mathbf{B}\|\langle 100\rangle$ and a microwave power of 1 μW. The signals denoted by an asterisk are due to impurities in a cavity. Arrows show the resonance fields of the sextet.

(see Fig. 2). The *B* signal observed at 5 K consists of six lines. The asterisk signals are due to impurities in a cavity as well as in Fig. 2. The separation fields between the adjacent lines are almost equal to 18 mT and increase slightly in increasing the resonance fields. The width of the fourth line at 0.35 T is the narrowest in the six lines.

Although the *i*th ($i=1,2,3,5,6$) lines measured at 5 K have only positive components, the fourth line has a week negative component. The line shapes of these six lines change from asymmetry to symmetry in increasing temperatures. The peaks of the positive components at 5 K are coincident with the resonance fields at 100 K.[11] The widths of the other five lines become broader away from the fourth line. These facts indicate that the spin-relaxation rate of the fourth line is much faster than those of the other five lines. Then, another single sharp line seems to be superimposed on the fourth line at 0.35 T. Contrary to this expectation, the angular variation of the six lines in the (010) plane in Fig. 5 shows no splitting of the fourth line and all six resonance fields remain constant in the (001) plane (not shown). Further, the intensity ratio of the six lines at 40 K calculated by twice integration of the first derivative curve is obtained to be 0.9:0.9:1:1:0.9:0.8 being close to 1:1:1:1:1:1. These facts lead to the opposite sense that the six lines of the *B* center is due to a single center. The detail of the *B* center is further discussed in the following paragraph.

The ESR measurements were carried out after the sample was annealed at 300 °C for 1 h. The broad *A* signal due to Ce^{3+} was observed at low temperatures. However, the sharp *B* signal could not be observed in the temperature range of 5–300 K, that is, the *B* center disappeared through the annealing treatment. The annealed sample was excited with the 355-nm laser light for half an hour at 293 K. The *B* signal was again observed at 293 K after the UV excitation. When the sample temperature was decreased down to 77 K, new ESR lines other than the *B* signal appeared. Figure 6 shows

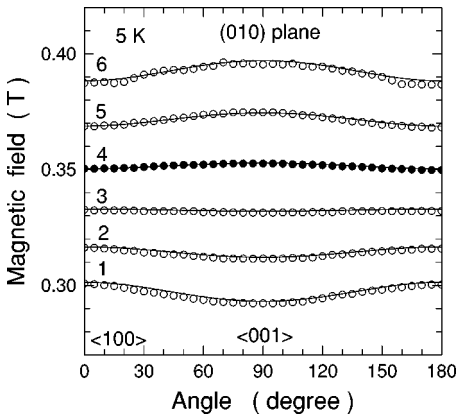

FIG. 5. The angular variation of the sextet of the *B* signal for $Ca_2Al_2SiO_7$:Ce at 5 K in the (010) plane. There is no splitting of the fourth resonance field denoted by solid circles. The solid curves are calculated using Eqs. (1) and (2) and the parameters of the *B* center in Table I.

the ESR spectra with $\mathbf{B}\|\langle 001\rangle$, $\langle 110\rangle$, and $\langle 100\rangle$. The lines numbered by 3, 4, and 5 are the components of the *B* signal in Fig. 4. The six lines with $\mathbf{B}\|\langle 100\rangle$, being denoted by *C*, have the intervals ($\sim$1 mT) between the adjacent lines, which are an order of magnitude smaller than for the *B* signal ($\sim$18 mT). The *C* signal with $\mathbf{B}\|\langle 001\rangle$ is unresolved and less intense, whereas that with $\mathbf{B}\|\langle 110\rangle$ is split into several sharp lines.

The angular variations of the *C* signals in the (010) and (001) planes were observed. Figure 7 shows the angular variation of the *C* signal in the (001) plane. The maximum splitting occurs when $\mathbf{B}\|\langle 110\rangle$. The *C* signal is composed of two sextets. Each line of the sextet in Fig. 7 is further split

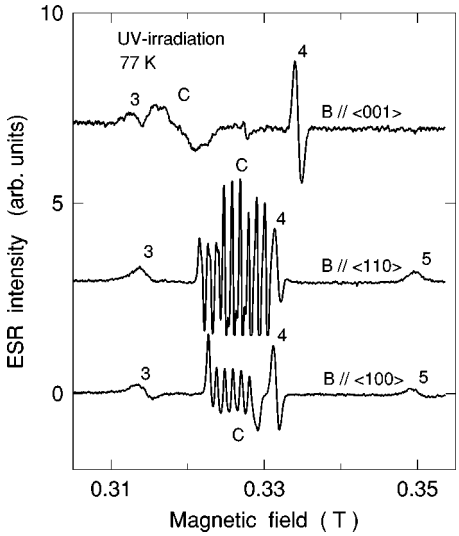

FIG. 6. After UV irradiation at 355 nm for half an hour at 293 K, the sample temperature was decreased down to 77 K. The ESR spectra for $Ca_2Al_2SiO_7$:Ce were measured with $\mathbf{B}\|\langle 001\rangle$, $\langle 110\rangle$, and $\langle 100\rangle$. The new *C* signal with $\mathbf{B}\|\langle 100\rangle$ is composed of six lines as well as the *B* signal. The numbers 3, 4, and 5 represent the components of the *B* signal (see Fig. 4).

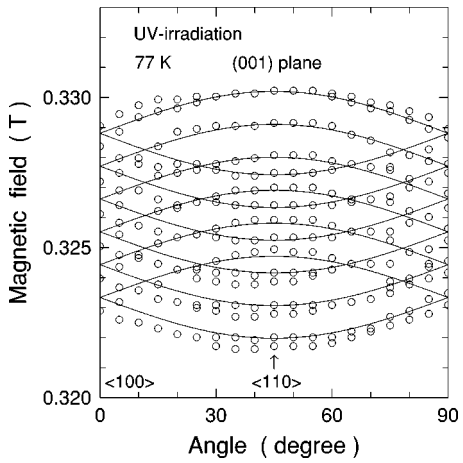

FIG. 7. The angular variation of the *C* signal for $Ca_2Al_2SiO_7$:Ce at 77 K in the (001) plane. The solid curves are calculated using Eqs. (1) and (2) and the parameters of the *C* center in Table I.

into two components due to small misalignment between the magnetic field and the crystalline (001) plane.

The angular dependence of the *B* and *C* signals fits curves calculated using the spin Hamiltonian of Eq. (1) including the hyperfine (h.f.) interaction in the form[12]

$$\mathcal{H}_{\text{h.f.}} = A_x I_x S_x + A_y I_y S_y + A_z I_z S_z , \tag{2}$$

where I is a nuclear spin and A_i $(i=x,y,z)$ is a hyperfine coupling constant. The principal z axes for *B* and *C* centers are experimentally determined to be parallel to $\langle 001 \rangle$ and $\langle 110 \rangle$, respectively. The g values of *B* and *C* centers are calculated taking account of the second-order perturbation of the hyperfine interaction.[12] The solid curves in Figs. 5 and 7 calculated using Eqs. (1) and (2) and the parameters of *B* and *C* centers in Table I fit the observed data points.

The nuclear spin of $I=5/2$ can be estimated from the six-hyperfine-line patterns $(2I+1)$ of *B* and *C* centers. The nuclear spins of the compositions ^{43}Ca, ^{27}Al, and ^{29}Si, with natural abundances of 0.13, 100, and 4.7 %, respectively, are 7/2, 5/2, and 1/2. Therefore, *B* and *C* centers are strongly associated with the nuclear spin of ^{27}Al. The large difference in the magnitude of the hyperfine coupling constants for *B* and *C* centers can be explained by the valence of Al. The detail will be discussed in Sec. IV.

B. Optical measurements

The optical absorption spectrum of Ce^{3+} in the as-grown CASM crystal measured at 293 K is shown in Fig. 8(a). The spectrum consists of overlapping broadbands below 360 nm. After annealing the sample at 300 °C for 1 h, the absorption coefficients decrease below 330 nm and the absorption spectrum is clearly resolved into five bands with peaks at 228, 244, 278, 300, and 352 nm in Fig. 8(a). These five bands correspond to the five energy levels of $5d$ excited states of Ce^{3+} in the crystal because Ce^{3+} complexes with C_s symmetry have the five nondegenerated $5d$ orbitals.[1,13] The difference between the absorption spectra of the as-grown and

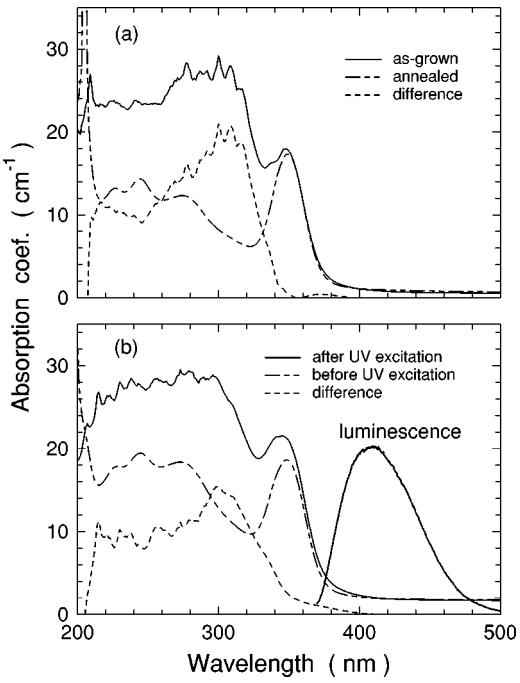

FIG. 8. (a) The absorption spectra of the as-grown and annealed crystals $Ca_2Al_2SiO_7$:Ce. The dashed curve represents their difference. (b) The absorption spectra of the annealed crystal $Ca_2Al_2SiO_7$:Ce before and after UV excitation. The dashed curve represents their difference. The Ce^{3+} luminescence spectrum excited at 355 nm is added in (b).

annealed samples is represented by a dashed line in figures. The difference spectrum is composed of an intense broadband with a peak at ~300 nm and strong and weak tails at both sides of short and long wavelengths, respectively.[8] The annealed sample was excited with the 355-nm laser light for half an hour. The optical absorption spectrum [Fig. 8(b)] is changed to be similar to that of the as-grown sample [Fig. 8(a)]. The difference spectrum between the absorption spectra of the annealed sample before and after the UV excitation is also represented by a dashed curve. These results indicate strongly that both difference spectra are associated with *B* and/or *C* centers observed using the ESR technique.

Steady-state excitation at 350 nm produces broadband luminescence with a peak at 410 nm, being due to the $5d \rightarrow 4f$ transition of Ce^{3+} as shown in Fig. 8(b). The luminescence band has a tail to longer wavelengths created by inhomogeneous broadening and overlapping two bands from the transitions to the $^2F_{5/2}$ and $^2F_{7/2}$ ground state of Ce^{3+}.[13] The line shape of the phosphorescence spectrum after the removal of the UV excitation at 293 K is coincident with that of the luminescence obtained under the steady-state UV excitation in Fig. 8(b). This gives evidence that the phosphorescence occurs at Ce^{3+} sites.

Figure 9 shows the temperature dependence of the radiative decay curves at the peak wavelength (410 nm) of the Ce^{3+} luminescence in the time range of 0–250 ns. The intrinsic radiative decay of Ce^{3+} was observed with a constant lifetime of 40 ns in the temperature range of 77–400 K, which is due to the allowed electric-dipole $5d \rightarrow 4f$ transition. The lifetime is close to 65 ns for YAG:Ce^{3+} (Ref. 5)

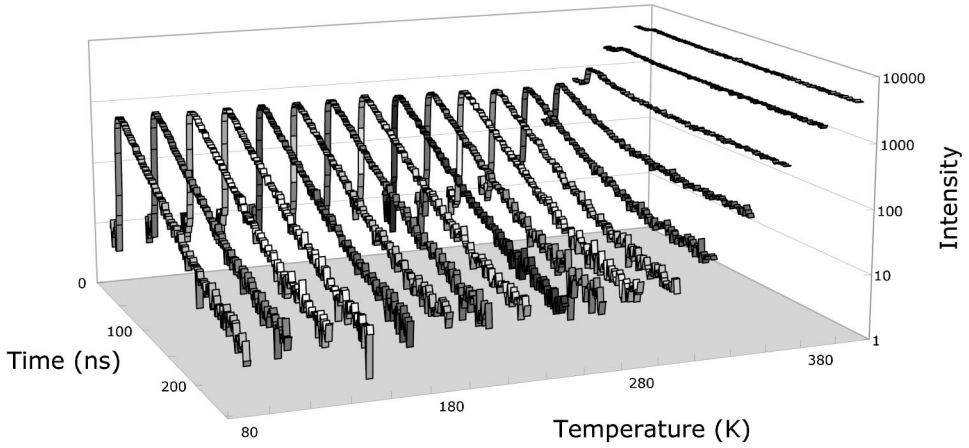

FIG. 9. The temperature dependence of the radiative decay curves of the luminescence at 410 nm in $Ca_2Al_2SiO_7$:Ce excited at 355 nm in the time range of 0-250 ns. The background intensities increase drastically above 300 K.

and 25 ns for $LiCaAlF_6:Ce^{3+}$.[4] The intensities of the intrinsic components are constant below ~300 K, gradually decreased and reduced to half an amount at 400 K. On the other hand, the background level at 400 K increases $\sim 10^3$ times larger than below 300 K. This result suggests that the components with long lifetimes are drastically enhanced as the temperature increases above 300 K.

Figure 10 shows the decay curves of the phosphorescence in the time range of $5-10^3$ s in log-log scales at $T=280$, 350, and 500 K. The decay curves below 280 K are almost the same as that at 280 K, and the intensities increase drastically above 300 K. The initial intensity ($t\sim 4$ s) measured at 500 K is about three orders of magnitude larger than that at 280 K. These results are in agreement with the increase of the background levels in Fig. 9. The decay curves fit the formula $I=a\times t^{-n}$, resulting in tunneling recombination between distant pairs of electron and hole in the crystal.[14–16]

Figure 11 shows the intensities of the phosphorescence integrated in the time range of $5-10^3$ s plotted as a function of $1/T$. In the higher temperature range ($T>300$ K), the intensities increase exponentially. The data points fit a curve calculated using the modified Arrhenius' equation in the form

$$I(T)=I_{\mathrm{tun}}+I_0\times\exp(-\Delta/k_BT), \tag{3}$$

where k_B is the Boltzmann constant, I_0 and I_{tun} are fitting parameters, and Δ is an activation energy. The fitting parameters are obtained to be $I_{\mathrm{tun}}=80$, $I_0=1.29\times 10^7$, and $\Delta=243$ meV.

As shown in Figs. 10 and 11, the phosphorescence intensities below 300 K are fairly weak compared with those above 300 K. This indicates that the excitation energy is stored in the crystal below 300 K and released above 300 K. The ESR results suggest that the energy is stored in the form of trapped electrons and holes. Then, there is a possibility that the energy stored at low temperatures is released through irradiation of a visible light, being associated with the transition to the excited state of either trapped electrons or holes. Such experiments were made in Si:Er by Gresorkiewicz.[17,18]

Figure 12 shows the decay curves of the phosphorescence when the first 355-nm laser light is removed at $t=0$ s and the second 633-nm He-Ne cw-laser light is turned on at $t=100$ s with various irradiation periods and a fixed temperature of 150 K. The shapes of the decay curves produced by the second cw excitation are very similar to those after the first UV excitation. The intensities are sharply cut when the light is turned off.

Figure 13 shows the temperature dependence of the decay curves with the first and second excitations when the second

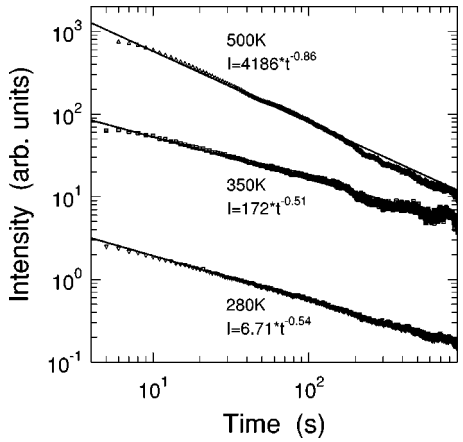

FIG. 10. The temperature dependence of the decay curves of the phosphorescence at 410 nm in $Ca_2Al_2SiO_7$:Ce measured at 280, 350, and 500 K in the time range of $5-10^3$ s. The straight lines are calculated by the least squares method.

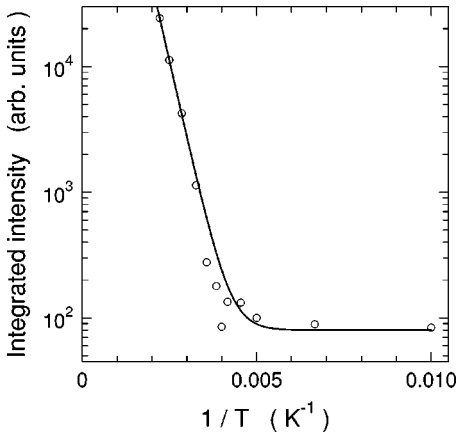

FIG. 11. The intensities of the phosphorescence integrated in a time domain plotted as a function of $1/T$. The solid curve calculated using Eq. (3) and the parameters of $I_0=80$, $I_{\mathrm{tun}}=1.29\times 10^7$, and $\Delta=243$ meV fits the observed data points.

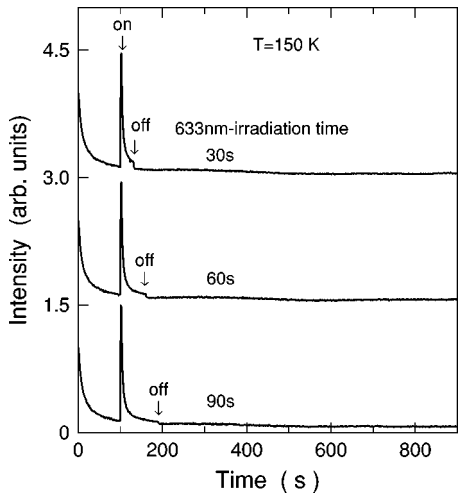

FIG. 12. The decay curves of the phosphorescence with first 355-nm excitation and second 633-nm cw excitation in various irradiation periods at 150 K.

cw light is turned on at $t=300$ s. The intensities of the second phosphorescence rapidly decrease above 70 K. The temperature dependence of the integrated second-phosphorescence intensities is shown in Fig. 14. The decrease of the intensities at higher temperatures may be due to nonradiative decay process. The transition probabilities including nonradiative decay process from the excited to ground states is given in the form[19]

$$I_r(T)=\frac{I_1}{1+R_{\mathrm{non}}\times\exp(-\Delta E/k_BT)}, \tag{4}$$

where I_1 and R_{non} are fitting parameters and ΔE is an activation energy corresponding to the nonradiative decay transition. The solid curve in Fig. 14 calculated using Eq. (4) and the parameters of $I_1=135$, $R_{\mathrm{non}}=5.7$, and $\Delta E=12$ meV fit the observed data points. This result shows that the nonradiative transition rate is faster than the energy transfer rate to Ce^{3+} sites, in increasing temperatures.

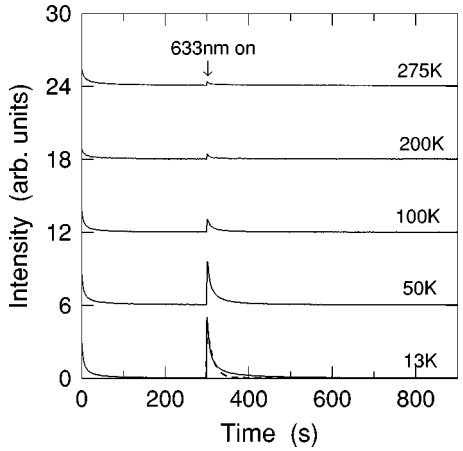

FIG. 13. The temperature dependence of the decay curves of the phosphorescence with the first and second excitations where the second light is turned on at $t=300$ s and keeps on. The decay curve at 13 K fits a dashed curve calculated using Eq. (11) and the parameters of $\lambda_1=2.38$, $\lambda_2=0.070$, $\beta_1=-5.0$, and $\beta_2=4.9$.

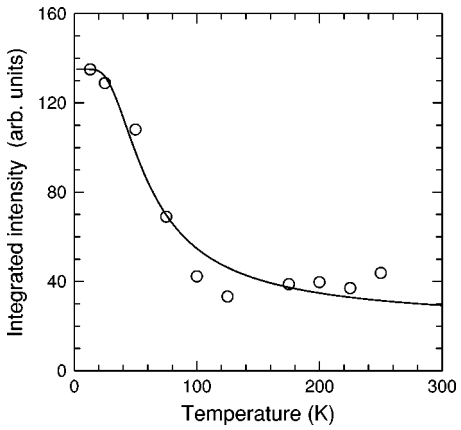

FIG. 14. The integrated second-phosphorescence intensities as a function of temperature. The solid curve is calculated using Eq. (4) and the activation energy of $\Delta E=12$ meV.

Figure 15 shows the relation between the UV excitation power P_n and the integrated intensity of the phosphorescence I_n which are normalized by the maximum power and the maximum intensity, respectively. The observed data points lie on a straight line represented by $I_n=\sqrt{P_n}$. This result indicates that pairs of electron and hole are created by a one-photon process and that they are trapped at stable sites, thermally released from them and recombine radiatively at Ce^{3+} sites.[17,18,20]

IV. DISCUSSION

A. Pairs of electron and hole produced by UV excitation

1. ESR

The energy levels of the $5d^1$ excited state of Ce^{3+} corresponding to the five absorption bands in the range of 200–370 nm are located into the band gap of the host CASM

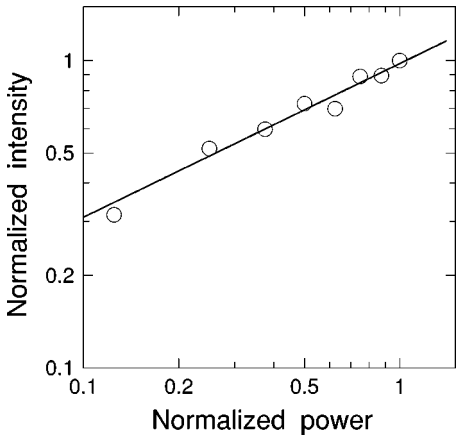

FIG. 15. The integrated phosphorescence intensities as a function of the UV excitation power. The power and intensity are normalized by the maximum power and the maximum intensity. The solid line with the slope of 1/2, being calculated by the least squares method, satisfies the equation of $I_n=\sqrt{P_n}$.

crystal. As the 355-nm excitation is not the band-to-band transition, it is difficult to produce directly pairs of electron and hole. However, the optical results suggest that the pairs are produced via the one-photon process, that is, the transition to the excited states of Ce^{3+}. According to the ESR results, the trapped electrons and holes are relatively stable below room temperature. It is very important to identify the local structure of the trapped electrons and holes in order to propose a mechanism of the long-lasting phosphorescence process, that is, how the UV energy is stored in the crystal, released, and emitted radiatively.

First, we discuss the spin Hamiltonian parameters of *B* and *C* centers in Table I being observed after the UV excitation. Their *g* values are very close to the free electron *g* value of $g_e=2.0023$, resulting in a singlet orbital with the electron spin of $S=\frac{1}{2}$. Positive and negative *g* shifts ($\Delta g=g-g_e$) are strongly associated with holes and electrons, respectively, because they are determined by the sign of the spin-orbit coupling constants [see Eq. (6)].[12,21] Then, *B* and *C* centers are expected to be assigned to electrons and holes from the observed *g* values, respectively.

Next, the local structure of these centers is discussed in terms of the hyperfine coupling constants. The six-hyperfine-line patterns ($2I+1$) of *B* and *C* centers are ascribed to the nuclear spin ($I=5/2$) of ^{27}Al. The observed *g* values ($g_x=2.052$, $g_y=2.016$, $g_z=2.000$) for the *C* center are in good agreement with those ($g_x=2.052$, $g_y=2.015$, $g_z=2.005$) of the oxygen-hole aluminum centers in the x-ray irradiated zircon $ZrSiO_4$.[22] The hyperfine coupling constants of ($|A_x|=25$ MHz, $|A_y|=|A_z|=31$ MHz) for *C* center are slightly larger than those ($A_x=-19$ MHz, $A_y=-22$ MHz, $A_z=-23$ MHz) for zircon. The larger hyperfine coupling constant is associated with the larger electron density at the nuclear position. Then, the holes for the *C* center are expected to be localized at Al sites more efficiently than those for the oxygen-hole aluminum centers in zircon. If the holes are shared between O^{2-} and Al^{3+} as the same as in zircon, there are many configurations of the holes with various O^{2-}-Al^{3+} bonding axes. However, the ESR results show only two configurations with the principal *z* axes of $\langle 110\rangle$ and $\langle \bar{1}10\rangle$ normal to each other. The two principal *z* axes are equal to the lines joining Al(2) and Si ions in Fig. 1(a). The ICP analyses show the $\sim$10% concentration of Si^{4+} vacancies in the crystal. These facts deduce that the holes produced in CASM are attracted around Si^{4+} vacancies and self-trapped at Al^{3+} ions by the electron-phonon interaction, forming Al^{4+} complexes accompanied by Si^{4+} vacancies along the $\langle 110\rangle$ or $\langle \bar{1}10\rangle$ direction. As a consequence, the holes produced in CASM are self-trapped at the Al(2) sites.

The ground configuration $1s^22s^22p^5$ of the self-trapped holes Al^{4+} is as the same as O^-. The energy levels and the *g* tensors of trapped holes O^- in oxides were studied experimentally and theoretically.[23] A ^2P state splits into an orbital singlet $^2P(A)$ and an orbital doublet $^2P(E)$, for example, in axially symmetric crystal field, corresponding to the ground and first excited states. Optical absorption due to the transition $^2P(A)\rightarrow{}^2P(E)$ occurs at a photon energy of $\Delta_p=E[^2P(E)]-E[^2P(A)]$ in the visible range. The *g* values calculated through the second-order perturbation of the spin-orbit interaction are given by

$$g_{\parallel}=g_e, \tag{5}$$

$$g_{\perp}=g_e\left(1-\frac{\lambda}{\Delta_p}\right), \tag{6}$$

where λ is the spin-orbit coupling constant for O^- ($\lambda<0$).[12,21–24] The *g* tensor of the *C* center is orthorhombic. The observed value of $g_z=2.000$ is in good agreement with that of $g_{\parallel}$ in Eq. (5). The average value of g_x and g_y is set to $g_{\perp}$ in Eq. (6). The *g* shift of $g_{\perp}$ in Eq. (6) can be estimated to be $\lambda/\Delta_p=-0.016$. If the value of λ is assumed to be equal to that (-135 cm^{-1}) of O^-,[23] the energy Δ_p is roughly estimated to be 8400 cm^{-1}, being associated with the near infrared region.

Next, let us identify the *B* center. The hyperfine coupling constants for the *B* center in Table I are an order of magnitude larger than for the *C* center, so that the *B* center cannot be assigned to another self-trapped hole Al^{4+} without Si^{4+} vacancies. The large difference in the hyperfine coupling constants of the *B* and *C* centers can be explained by the different valence states of Al, that is, *p* and *s* orbitals, where the *s* orbital has a much larger electron density at the nuclear position than the *p* orbital. The observed values ($|A_{\parallel}|=590$ MHz and $|A_{\perp}|=490$ MHz) are nearly equal to half the amount of that (1170 MHz) for the $^2S_{1/2}$ state of Al^{2+} in Si crystals.[21] This suggests that the electron density at the nuclear position of Al in CASM is less than in Si, that is, the electron wave function extends out of the Al ion. If the electrons are assumed to be localized at Al^{3+}, the Al^{3+} ions could act as both of electron and hole centers. This explanation leads to the difficulty of how to distinguish trapping processes of electrons and holes. In addition to this discrepancy, the *B* center has the strange ESR feature. The width of the fourth line in Fig. 4 is narrower than those of the other five lines, which become broader away from the fourth line. The resonance fields of the fourth line give $g_{\parallel}=1.960$ and $g_{\perp}=1.974$, being very close to those of F^+ centers in simple oxides CaO, SrO, and BaO.[23] These results lead to a possibility that the *B* center may be assigned to electrons trapped at O^{2-} vacancies in the form of F^+ centers.

We consider further where the O^{2-} vacancy is created at three different O(1), O(2), and O(3) sites in the CASM crystal as shown in Fig. 1. The CASM crystal has a (001) cleaved face. The O(1) and O(3) ions make bonding in the (001) plane, whereas the O(2) ion does not bond in the (001) plane. In addition, only the direction of O(2)-Al(2) except O(1)-Al(2), O(3)-Al(2), and O(3)-Al(1) is parallel to the $\langle 001\rangle$ axis, being coincident with the principal *z* axis of the *B* center. Taking account of these facts, O^{2-} vacancies are expected to be produced preferentially at the O(2) sites. Then, the *B* center is assigned to a single electron trapped at the O(2) vacancy such as the F^+ center, the wave function extending toward the Al(2) ion along the $\langle 001\rangle$ direction.

The assignment of *B* and *C* centers suggests that the aluminum ions accompanied by the vacancies of Si^{4+} or O^{2-} at the nearest neighbors play an important role for trapping

holes or electrons, respectively. In order to understand the more detailed structures of these centers, a further ESR measurement, for example, a high frequency ESR measurement and calculation of the electronic energy levels and wave functions of the clusters consisting of trapped electrons (holes) and the surrounding ions in CASM are required.

2. Optical absorption

We consider a relaxation process of electron-hole pairs produced in the CASM crystal by the UV excitation of Ce^{3+}. The UV light excites the $4f$ electron of Ce^{3+} to the $5d$ energy levels. The excited electron is expected to be transferred to the nearby O^{2-} vacancy created at the O(2) sites, for example, through downward hopping. The electron immediately relaxes to the stable states and is trapped as F^+ center. On the other hand, the hole produced at Ce^{3+} by the UV excitation moves toward a Si^{4+} vacancy and is self-trapped at an Al(2) site, forming Al^{4+} through the electron-phonon interaction. Such trapped electron and self-trapped hole are strongly associated with the O^{2-} and Si^{4+} vacancies produced under the crystal growth process.

The difference spectra in Fig. 8 consist of the intense bands with the double peaks at 283 and 302 nm and an intense background below 270 nm.[8] The absorption spectra of F^+ centers in MgO, CaO, SrO (Ref. 23) and Al_2O_3 (Ref. 25) have peaks at 250, 340, 400, and 250 nm, respectively. Their spectra have double-peak structures in the UV range. Especially, the spectrum of F^+ centers in Al_2O_3 is resolved into two peaks clearly, being assigned to the transitions between $1s$- and $2p$-like states in analogy to the hydrogen atom.[25] As the large absorption coefficients are due to spin- and parity-allowed transitions, the difference spectrum observed in the UV range is assigned to the electrons trapped at O^{2-} vacancies such as F^+ centers.

In the same way, the absorption spectrum of the self-trapped holes Al^{4+} is expected to be similar to that of O^-, which is assigned to $2p_z \rightarrow 2p_x, 2p_y$ transitions in the visible and near infrared ranges. The transitions are parity forbidden, resulting in small absorption coefficients.[23] Although the visible absorption was not clearly observed in the difference spectra in Fig. 8, the second visible excitation enhanced the phosphorescence in a pulse shape as shown in Figs. 12 and 13. Therefore, the visible excitation may be due to the optical transition of the self-trapped hole Al^{4+} to the excited state with small transition probabilities.

B. A model of long-lasting phosphorescence process

The line shape of the phosphorescence with long lifetimes (1-10^3 s) is the same as that of the intrinsic Ce^{3+} luminescence with the lifetime of 40 ns. The decay curves of the phosphorescence intensity at various temperatures satisfy the equation of $I(t)=I_0 t^{-n}$ $(n<1)$ calculated in terms of tunneling between trapped holes and electrons.[14–16] The temperature dependence of the integrated intensity obeys the Arrhenius' equation.[26]

These results suggest the following process for the phosphorescence.

(1) Pairs of electrons and holes are produced at Ce^{3+} ions by the UV excitation of Ce^{3+} and move to stable trapped sites. The electrons are trapped at O^{2-} vacancies such as F^+ centers, while the holes are self-trapped at Al^{3+} near to Si^{4+} vacancies, forming Al^{4+}.

(2) The holes move back to Ce^{3+} in the crystal by thermal and optical excitation. The holes are retrapped at Ce^{3+} and recombine the trapped electrons radiatively by tunneling. Then, the phosphorescence has the same line shape of the intrinsic Ce^{3+} luminescence.

There is another possible process for (2): trapped electrons move to Ce^{3+} sites, forming Ce^{2+}. However, it may be excluded because the energy level of Ce^{2+} is expected to be much higher than those of the excited state of Ce^{3+}.[27,28] Here, we discuss the above process (2) in detail, that is, how the holes move back to Ce^{3+} by thermal and optical excitation. The integrated phosphorescence intensities are drastically increased above 300 K. The intensities as a function of $1/T$ in Fig. 11 satisfy the Arrhenius' equation in Eq. (3). The first term in Eq. (3) represents the transfer of holes from Al to Ce sites by tunneling. Tunneling is independent of temperatures and occurs dominantly at low temperatures. The second term represents hopping motion with the activation energy of 243 meV.[26] It is strongly related to hopping between adjacent self-trapped-hole sites separated by a barrier.[14] The barrier height may be determined by the Si^{4+} vacancy.

Next, we consider the energy transfer process from the excited states of the self-trapped holes Al^{4+} to distant Ce^{3+} sites. The optical excitation of the self-trapped holes enhances effectively the phosphorescence at low temperatures below 70 K. This suggests that the temperature dependence of the hole transfer via the excited states is reverse to that via the ground state by phonon-assisted hopping. These phenomena can be interpreted by assuming a model that the excited holes may move in the crystal until they are either re-self-trapped at Al^{3+} or trapped at Ce^{3+}. This process is simply illustrated using a three-energy-level scheme. The population numbers of self-trapped holes of Al^{4+} in the ground and excited states are n_1 and n_2, respectively, whereas that of holes trapped at Ce^{3+} is n_3. The rate equations can be given by[29]

$$\frac{dn_1}{dt} = -W_{12}n_1 + W_{21}n_2, \tag{7}$$

$$\frac{dn_2}{dt} = W_{12}n_1 - (W_{23} + W_{21})n_2, \tag{8}$$

$$\frac{dn_3}{dt} = W_{23}n_2, \tag{9}$$

where W_{ij} is the $i \rightarrow j$ transition probability. W_{12} is the optical transition of self-trapped holes Al^{4+} to the excited state corresponding to the second visible excitation in Figs. 12 and 13. The solutions of the rate equations are, in general, described in forms[29]

$$n_1(t) = \alpha_1 \exp(-\lambda_1 t) + \alpha_2 \exp(-\lambda_2 t), \tag{10}$$

$$n_2(t)=\beta_1\exp(-\lambda_1 t)+\beta_2\exp(-\lambda_2 t), \tag{11}$$

$$\lambda_1+\lambda_2=W_{12}+W_{21}+W_{23}, \tag{12}$$

$$\lambda_1\lambda_2=W_{12}W_{23}. \tag{13}$$

Here, α_i and β_i $(i=1,2)$ are constants determined by the initial conditions of the experiments and given by

$$n_1(0)=\alpha_1+\alpha_2=N, \tag{14}$$

$$n_2(0)=\beta_1+\beta_2=0, \tag{15}$$

$$n_3(0)=0. \tag{16}$$

The transition probabilities W_{ij} represented using the constants α_i, β_i and λ_i $(i=1,2)$ are given by

$$W_{12}=\frac{\beta_2}{\alpha_2+\beta_2}\lambda_1, \tag{17}$$

$$W_{21}=\frac{\alpha_2}{\alpha_2+\beta_2}\lambda_1-\frac{\alpha_2}{\beta_2}\lambda_2, \tag{18}$$

$$W_{23}=\frac{\alpha_2+\beta_2}{\beta_2}\lambda_2. \tag{19}$$

If the radiative decay rate of the phosphorescence due to recombination between Ce^{4+} and a trapped electron is assumed to be much larger than W_{23}, the decay rate is proportional to dn_3/dt in Eq. (9). The observed decay curve for the second 633-nm cw excitation at 13 K in Fig. 13 fits the dashed curve calculated using Eq. (11) with parameters of $\lambda_1=2.38$, $\lambda_2=0.070$, $\beta_1=-5.0$, and $\beta_2=4.9$, where the values of β_1 and β_2 nearly satisfy Eq. (15). The single exponential curve deviates largely from the tail of the observed curve. The disagreement may be removed by a distribution of W_{23} in terms of distances between self-trapped holes and Ce^{3+} ions.

In the case of $W_{21}\ll W_{23}$, W_{12}, and W_{23} in Eqs. (17) and (19) become λ_1 and λ_2, respectively. Therefore, the rapid increase and gradual decrease rates of the phosphorescence intensity induced by the second cw excitation are equal to W_{12} and W_{23}, respectively. The temperature dependence of the second decay curves in Fig. 13 indicates that W_{21} increases as temperatures increase, that is, the excited holes relax to the ground state nonradiatively through a multiphonon emission process.

V. CONCLUSIONS

The UV excitation of Ce^{3+} in the CASM crystal produces the long-lasting phosphorescence with the distribution of the radiative decay rates. The excitation energy is stored in the crystal below 300 K and gradually released above 300 K. The ESR results indicate that the energy is stored in the forms of the electrons trapped at O^{2-} vacancies such as F^+ centers and the holes self-trapped at Al^{3+} near to Si^{4+} vacancies, forming Al^{4+}.

In the previous paper,[8] the properties of the phosphorescence from the Ce^{3+}-doped $CaYAl_2O_7$ (CYAM) crystal with the same melilite crystal structure were reported. The thermoluminescence curves of the CASM:Ce and CYAM:Ce crystals as a function of temperature show broadbands with maxima of the intensities at 370 and 90 °C, respectively. The activation energy for the CYAM:Ce crystal was obtained to be 131 meV. The higher temperature corresponds to the larger activation energy. In the case of CASM, the holes are self-trapped as Al^{4+} accompanied by a Si vacancy. On the other hand, the holes in the CYAM may be self-trapped at an Al^{3+} ion without an Al^{3+} vacancy, because the activation energy of CYAM is half an amount of that for CASM. In consequence, the vacancies or some defects in CASM:Ce and CYAM:Ce modify the barrier height between the self-trapped holes.

Matsuzawa *et al.*[6] reported the long-lasting phosphorescence using alkaline-earth aluminates $Sr_4Al_{14}O_{25}:Eu^{2+}:Dy^{3+}$ and $SrAl_2O_4:Eu^{2+}:Dy^{3+}$. They proposed that the phosphorescence occurs through recombination of electron-hole pairs created by optical excitation, where Dy^{3+} plays a role as a hole-trapped center. According to our model of the phosphorescence for CASM:Ce, there is a possibility that a hole is not trapped at Dy^{3+}, but self-trapped at Al^{3+} and that Dy^{3+} affects the barrier height between the self-trapped holes in the crystals as well as the Si^{4+} vacancies in CASM.

ACKNOWLEDGMENTS

This work was in part supported by a Grant-in-Aid for Science Research (C) from the Japan Society for the Promotion of Science (Grant Nos. 12650665, 14550037). One of the authors (M.Y.) is indebted to the Iketani Science and Technology Foundation for a research grant.

[1] G. Blasse and B. C. Grabmaier, *Luminescent Materials* (Springer, Berlin, 1994).

[2] P. Moulton, *Laser Handbook*, edited by M. Bass and M. H. Stitch (North-Holland, Amsterdam, 1985), Vol. 5, p 282.

[3] T.D.J. Ehrlich, P.F. Moulton, and R.M. Osgood, Opt. Lett. **4**, 184 (1978).

[4] C.D. Marshall, J.A. Speth, S.A. Payne, W.F. Krupke, G.J. Quarles, V. Castillo, and B.H.T. Chai, J. Opt. Soc. Am. B **11**, 2054 (1994).

[5] D.S. Hamilton, S.K. Gayen, G.J. Pogatshnik, R.D. Ghen, and W.J. Miniscalco, Phys. Rev. B **39**, 8807 (1989).

[6] T. Matsuzawa, Y. Aoki, N. Takeuchi, and Y. Murayama, J. Electrochem. Soc. **143**, 2670 (1996).

[7] N. Kodama, M. Yamaga, and T. Kurahashi, Radiat. Eff. Defects Solids **151**, 159 (1999).

[8] N. Kodama, T. Takahashi, M. Yamaga, Y. Tanii, J. Qiu, and K.

Hirao, Appl. Phys. Lett. **75**, 1715 (1999).
[9] S.J. Louisnathan, Can. Mineral. **10**, 822 (1971).
[10] M. Weger, Bell Syst. Tech. J. **39**, 1013 (1960).
[11] M. Yamaga, N. Kodama, T. Yosida, B. Henderson, and K. Kindo, J. Phys.: Condens. Matter **9**, 9639 (1997).
[12] J. R. Pilbrow, *Transition Ion Electron Paramagnetic Resonance* (Clarendon, Oxford, 1990).
[13] N. Kodama, M. Yamaga, and B. Henderson, J. Phys.: Condens. Matter **8**, 3505 (1996).
[14] C.J. Delbecq, Y. Toyozawa, and P.H. Yuster, Phys. Rev. B **7**, 4497 (1974).
[15] T. Tashiro, S. Takeuchi, M. Saidoh, and N. Itoh, Phys. Status Solidi B **92**, 611 (1979).
[16] M. Iwanaga, M. Watanabe, and T. Hayashi, Phys. Rev. B **62**, 10 766 (2000).
[17] T. Gregorkiewicz, D.T.X. Tha, and J.M. Langer, Appl. Phys. Lett. **75**, 4121 (1999).
[18] T. Gregorkiewicz, D.T.X. Tha, J.M. Langer, H.H.P.Th. Bekman, M.S. Bresler, J. Michel, and L.C. Kimerling, Phys. Rev. B **61**, 5369 (2000).
[19] M. Yamaga, Y. Gao, F. Rasheed, K.P. O'Donnell, B. Henderson, and B. Cockayne, Appl. Phys. B: Photophys. Laser Chem. **51**, 329 (1990).
[20] J. Palm, F. Gan, B. Zheng, J. Michel, and L.C. Kimerling, Phys. Rev. B **54**, 17 603 (1996).
[21] G. E. Pake and T. L. Estle, *The Physical Principles of Electron Paramagnetic Resonance* (Benjamin, London, 1973), Chap. 10.
[22] R.F.C. Claridge, K.M. Mackle, G.L.A. Sutton, and W.C. Tennant, J. Phys.: Condens. Matter **6**, 10 415 (1994).
[23] A. E. Hughes and B. Henderson, in *General and Ionic Crystal*, edited by J. H. Crawford and L. M. Slifkin, Vol. 1 of *Point Deffects in Solids* (Plenum, New York, 1972), Chap. 7.
[24] R.F.C. Claridge, N.S. Lees, W.C. Tennant, and C.J. Walsby, J. Phys.: Condens. Matter **12**, 1431 (2000).
[25] B.D. Evans and M. Stapelbroek, Phys. Rev. B **18**, 7089 (1978).
[26] P.J. Ventura, M.C. do Carmo, and K.P. O'Donnell, J. Appl. Phys. **77**, 323 (1995).
[27] G.J. Hollingsworth and D.S. McClure, Phys. Rev. B **48**, 13 280 (1993).
[28] E. Radzhabov, J. Phys.: Condens. Matter **13**, 10 995 (2001).
[29] M. Fukui, Y. Hayashi, and H. Yoshioka, J. Phys. Soc. Jpn. **34**, 1226 (1973).